Environmental Science Nano

ROYAL SOCIETY OF CHEMISTRY

PAPER

View Article Online
View Journal | View Issue

Cite this: *Environ. Sci.: Nano*, 2023, **10**, 3423

Montmorillonite helps BiOCl photodegradation of antibiotics†

Gang Wang,[a] Shilin Zhang,[ac] Hongxiu Lu,[a] Chang Lu,[b] Mei Yang,[a] Kai Tang[a] and Aidong Tang *[ac]

Constructing efficient photocatalysts for the degradation of antibiotics was highly challenging. The support carrier played an active role in the reactivity, adsorption and lifetime of the catalyst. Herein, BiOCl/Mt photocatalysts were successfully prepared on a large scale by mixing natural iron-rich montmorillonite (Mt), bismuth nitrate, ethylene glycol (EG) and deionized water at room temperature. The optimal mass ratio of BiOCl/Mt was 1 : 1, and it could degrade 95.9% tetracycline hydrochloride (TCH) within 60 minutes. Compared with that of pure BiOCl, the degradation rate and kinetic constant were increased by 39% and 3.4 times, respectively. This was due to the fact that BiOCl/Mt has a smaller band gap and more positive valence potential than pure BiOCl, indicating a higher utilization efficiency of light and a stronger oxidation capability of holes (h^+). The leading role of holes in TCH degradation was confirmed by free radical trapping experiments. In addition, the potential intermediates were identified by liquid chromatography-mass spectrometry, and ECOSAR software predicted that more than half of the products were less toxic than TCH molecules. This study demonstrated that iron-rich Mt not only was a carrier but also participated in the photocatalytic reaction as a p-type semiconductor and formed a p–n heterojunction with n-type semiconductor BiOCl, which significantly improved the photocatalytic ability of BiOCl/Mt.

Received 27th August 2023,
Accepted 24th October 2023

DOI: 10.1039/d3en00582h

rsc.li/es-nano

Environmental significance

In recent years, the problem of water pollution caused by the abuse and misuse of antibiotics has become extremely serious, and the emergence of "superbugs" due to bacterial drug resistance is likely to render humans drug-free in the future. As a broad-spectrum antibiotic, tetracycline hydrochloride (TCH) is widely used in various fields. Therefore, the efficient degradation of TCH by photocatalytic technology is important for the purification of the water environment. Here, we successfully loaded BiOCl nanosheets on the natural iron-rich clay mineral montmorillonite (Mt) using a low-energy synthesis method. The composites with optimized loadings degraded 95.9% TCH within 60 min, with 39% and 3.4-fold improvement in degradation efficiency and kinetics, respectively, compared to pure BiOCl. The improved performance can be attributed to the remarkable adsorption capacity of the composites for TCH and the excellent photogenerated carrier separation efficiency. This work provides an innovative strategy for the design of low-energy clay-based photocatalysts.

1 Introduction

Antibiotics have the ability to resist bacterial infections, but their overuse can lead to contamination of various water bodies.[1] Tetracycline hydrochloride (TCH), being a representative broad-spectrum antibiotic, finds extensive utilization in the domains of medical practice, aquaculture, and livestock nutrition among numerous other antibiotics.[2] Despite its valuable properties, TCH possesses a structurally stable composition comprising four aromatic rings, which presents challenges in terms of absorption and metabolism within both human and animal systems.[3] Currently, traditional methods for degrading TCH include membrane separation,[4] adsorption,[5] ion exchange,[6] electrocatalysis,[7] and biodegradation.[8] Among these, physical adsorption is not only expensive but can only simply adsorb pollutants without substantial degradation or mineralization.[9] Photocatalysis technology is known for its economic, energy-saving, and environmentally friendly features. By using photocatalysts, photogenerated electrons and holes are

[a] *College of Chemistry and Chemical Engineering, Central South University, Changsha 410083, China. E-mail: adtang@csu.edu.cn; Tel: +86 731 8887 9616*
[b] *College of Minerals Processing and Bioengineering, Central South University, Changsha 410083, China*
[c] *Engineering Research Center of Nano-Geomaterials of Ministry of Education, Laboratory of Advanced Mineral Materials, and Faculty of Materials Science and Chemistry, China University of Geosciences, Wuhan 430074, China*

† Electronic supplementary information (ESI) available. See DOI: https://doi.org/10.1039/d3en00582h

produced under sunlight, and further reactions generate active species that degrade TCH molecules into CO_2, H_2O, and other small molecule substances.[10] Hence, the utilization of photocatalysis technology emerges as a highly promising approach for addressing the issue of antibiotic pollution in water environments.

Among the various semiconductor photocatalysts, the high chemical stability, low toxicity, and ease of synthesis associated with bismuth oxychloride (BiOCl) have generated substantial interest among researchers.[11,12] Moreover, BiOCl consists of $[Bi_2O_2]^{2+}$ ionic layers interspersed with double Cl^- layers, and this unique layered structure allows for an internal electric field. Numerous studies have shown in great detail how this internal electric field greatly facilitates the separation and migration of photogenerated charge carriers.[13,14] Despite these advantages, BiOCl still faces many limitations in practical large-scale applications, such as high preparation costs, a small specific surface area, difficulty in separating photogenerated carriers and a weak ability for TCH adsorption. Therefore, it is necessary to use a carrier material with a larger surface area to support the photocatalyst to improve the overall efficiency of the photocatalytic process.

At present, clay minerals are considered as good carrier materials because of their low cost, strong ion exchange ability and large specific surface area.[15–17] For example, Mt as a carrier for photocatalysts could significantly improve the adsorption capacity of pollutants.[18,19] However, our previous study found excellent photocatalytic properties of kaolinite due to the isomorphic substitution of Fe atoms in natural iron-rich clay minerals, degrading 80% of RhB within 120 minutes, and systematically analyzed the differences in the photocatalytic properties of Al–O and Si–O sublayers.[20] Mt was composed of three-layer structural units, wherein each unit comprised two Si–O tetrahedral layers and one Al–O octahedral layer, and similar to kaolinite, the Si and Al atoms in the sublayers were isomorphically substituted by Fe atoms. Did Mt also possess such properties?

We developed a mild method for mass-preparing BiOCl/Mt composites by employing the electrostatic attraction between the negatively charged surface of Mt and positively charged $Bi(OCH_2CH_2OH)^{2+}$ ions, utilizing an open container setup and operating at room temperature. Notably, due to the gravitational effect of Mt, BiOCl/Mt composites can be easily collected using the decantation method. The photocatalytic degradation results showed that BiOCl/Mt had enhanced photocatalytic and adsorption capabilities for TCH. We reveal the p–n heterojunction that was created between iron-rich Mt and BiOCl for the first time. Upon photoexcitation, the photogenerated electrons produced by BiOCl rapidly migrate to Mt, increasing photogenerated carrier separation. At the same time, bandgap analysis showed that the composites utilized light more efficiently and that higher valence band potential could generate more oxidizing holes (h^+). Finally, radical capture experiments and ESR were utilized to determine the active species in the system as h^+, $^{\cdot}O_2^-$ and $^{\cdot}OH$, with h^+ dominating. The degradation intermediates and their related toxicity were identified using LC-MS, which showed that most of the intermediates were non-toxic and more than half of them were less toxic than TC molecules. This study provided evidence that clay minerals served not only as carrier support materials but also as semiconductors involved in photocatalytic reactions, and offered an innovative strategy for low-energy mass production of clay-based photocatalysts.

2 Experimental

2.1 Synthesis of photocatalysts

BiOCl/Mt composites were synthesised by an electrostatic gravitational method. Specifically, 0.485 g $Bi(NO_3)_3{\cdot}5H_2O$ was first added to a mixture of 15 mL EG and 12 mL deionized water and stirred vigorously for 10 min, at which point the system appeared colorless and transparent. Then different masses of Mt as described in Table S1† were added. The mixture was stirred well for 18 h until the system appeared as a homogeneous suspension. The system soon became milky white with the addition of 3 mL of 1 M NaCl solution, and stirring was continued for 10 min after that. Finally, the reaction system was allowed to rest at room temperature for a full hour, and then system delamination was clearly visible (Fig. S1†). The upper clear layer was removed to collect the precipitated product, which was repeatedly washed with deionized water and anhydrous ethanol three times before being dried in an oven for 12 h at 60 °C. The product was then ground into powder for characterization and photocatalytic performance study. The synthesized composites were defined as 3B/1M, 2B/1M, 1B/1M, 1B/2M, and 1B/3M, respectively, according to the amount of loaded Mt. For comparison, no other conditions were changed, only unloaded Mt was used to obtain pure BiOCl nanosheets.

2.2 Photocatalytic performance evaluation

This study used a 300 W xenon lamp to simulate the degradation of TCH under sunlight in order to assess the performance of the photocatalysts. To ensure the accuracy of the measurements, a constant temperature circulating bath was used to maintain the quartz beaker at a constant temperature (25 °C) and the distance between the xenon lamp and the reaction system was kept at approximately 15 cm. The following steps were taken during the photocatalytic degradation experiments: 100 mL of TCH with a C_0 = 20 mg L^{-1} concentration was introduced to the reaction vessel along with 20 mg of photocatalyst. To make sure the system attained adsorption–desorption equilibrium, the adsorption was conducted in complete darkness for 60 min. After that, the concentration of TCH in the solution was measured using a UV-vis spectrophotometer (Agilent Cary 100) by measuring the absorbance at the maximum absorption peak (357 nm) of TCH in the clarified solution after 3 mL of the suspension had been filtered off the catalyst through a 0.22 μm aqueous membrane every 10 min. The photocatalytic performance was

evaluated by C_t/C_0, and its kinetics were investigated by $-dc/dt = kt$, where C_t is the concentration corresponding to any t, t is the time, and k is the kinetic constant of the quasi-primary reaction. It is crucial to emphasize that each photocatalyst in the aforementioned degradation studies was tested in triplicate. The average results from the three replicate experiments were considered as the final outcomes, and error bars were utilized to represent the estimated errors or variations in the data.

For the cyclic experiments, to avoid mass loss during each test, we followed the method proposed by Guan *et al.*[21] In brief, multiple tests were conducted simultaneously, and after each test, every effort was made to collect all the photocatalysts. Although the mass of the photocatalysts was reduced in each test, the collected amount was always sufficient for the next cycle until the final test.

2.3 Additional experimental information

The ESI† contains further details in the Experimental section, such as the materials and reagents used throughout the experiment, details of the free radical trapping experiment, steps of the photoelectrochemical testing, and characterization data.

3 Results and discussion

3.1 Characterization of crystal structure, chemical composition, and morphology

The X-ray diffraction (XRD) pattern (Fig. 1a) of pure BiOCl confirms that the product was tetragonal phase BiOCl (JCPDS No.06-0249). The diffraction peaks observed at 12.00°, 24.13°, 25.88°, 32.5°, 33.47°, 36.58°, and 40.91° were successfully identified as the crystal planes (001), (002), (101), (110), (102), (003), and (112) of BiOCl, respectively. No signals corresponding to other phases or impurities were observed. Various diffraction peaks at 8.88°, 17.81°, 20.85°, and 26.63° were unique reflections of the pristine Mt crystal planes. In addition, other peaks at 20.86° and 26.64° were caused by impurities, mainly including quartz (JCPDS No.77-1060).[22] For 1B/1M, a two-phase structure belonging to Mt and BiOCl was observed, indicating that BiOCl was successfully anchored onto the Mt support.[23] The XRD peak intensity of a series of BiOCl/Mt composites gradually decreased with increasing Mt content (Fig. 1b), indicating the improved dispersion and reduced crystallinity of BiOCl on the Mt support.[18]

Fourier transform infrared (FT-IR) spectroscopy was used to analyze the chemical makeup and functional groups of Mt, BiOCl, and 1B/1M. For the Mt and 1B/1M samples, the strong absorption peaks at 452 and 1006 cm^{-1} were attributed to the bending and asymmetric stretching vibrations of the Si–O–Si bond, respectively (Fig. 1b), which were characteristic of the Si–O tetrahedral layers in Mt.[24] According to the results of the XRD investigation, the absorption peak seen at 796 cm^{-1} matched the skeletal vibration of quartz. Peaks at 692 and 877 cm^{-1} were attributed to the bending vibrations of Si–O–Al and AlFeOH, respectively.[25,26] Pure BiOCl exhibited a significant absorption peak at 504 cm^{-1} caused by the stretching vibration of the Bi–O bond,[27] and the bending vibration of the Al–O–Si bond was thought to be responsible for a significant absorption peak at 520 cm^{-1} in the original Mt.[28] The Al–O–Si peak underwent a slight red shift in the 1B/1M sample, indicating the interaction between BiOCl and Mt. The spectral shift could be explained by the induced effect of the Bi^{3+} and Cl atoms, which induced a Coulomb coupling force between O in the Al–O–Si bond and Bi^{3+} in

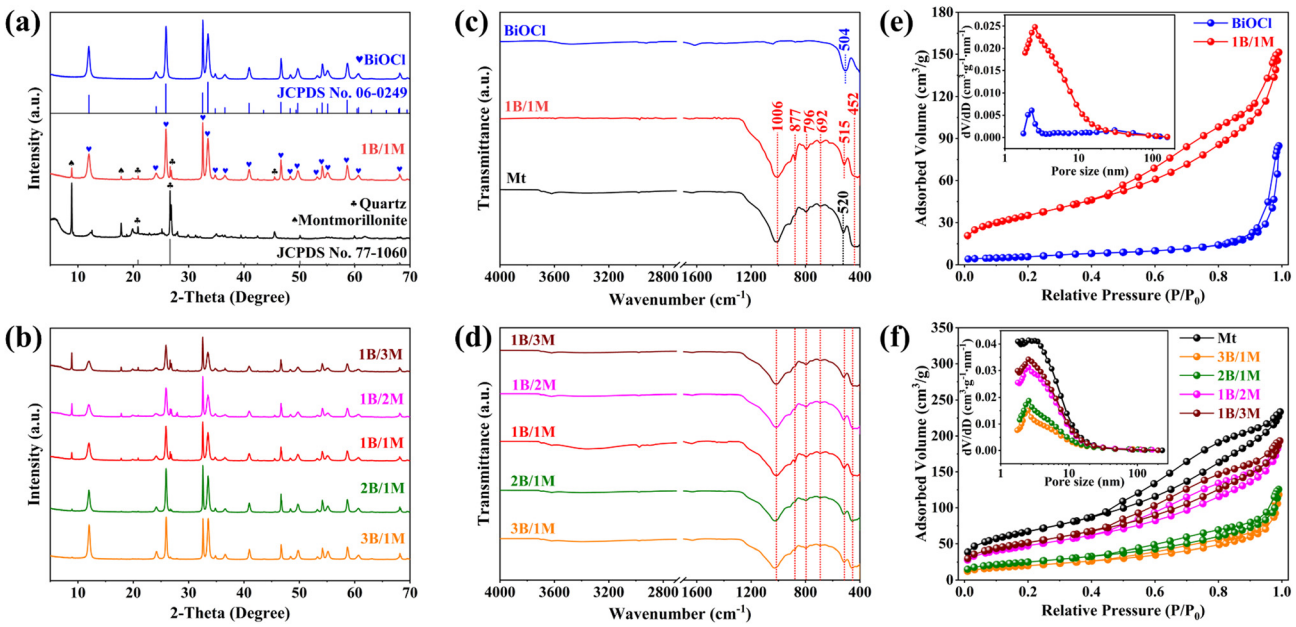

Fig. 1 (a and b) XRD patterns, (c and d) FTIR spectra and (e and f) N_2 adsorption–desorption isotherms and corresponding pore size distribution (inset) plots for all samples.

BiOCl.[29] At the same time, the Cl atom with a strong electron-withdrawing ability could also interact with the Al–O–Si bond, altering the charge distribution in the Al–O–Si bond and changing the force constant of the bond, resulting in a change in the vibrational frequency.[17,30] In addition, the FTIR spectra of other composite materials with different mass ratios are shown in Fig. 1d, where they are similar to that of 1B/1M without any significant differences.

Nitrogen adsorption–desorption isotherm curves were utilized to analyze the specific surface area and pore size distribution of the synthesised samples. In Fig. 1e, all samples were categorized as type IV isotherms with a distinct H3 hysteresis loop, which is characteristic of mesoporous materials.[31,32] The 1B/1M composite and BiOCl had specific surface areas of 126.38 and 21.96 $m^2\ g^{-1}$, respectively, which was an approximately 6-fold increase attributed to the Mt support. An increased specific surface area offered a greater number of active sites, thereby enhancing the photocatalytic efficiency.[33] For the 1B/1M composite material, its adsorption and desorption curves overlap in a relatively low-pressure region, a clear hysteresis loop appeared when the relative pressure exceeded 0.45, and its adsorption isotherm curve was steep in the relatively high-pressure region (P/P_0 >0.95). This information reaffirms that 1B/1M composite materials were predominantly mesoporous, as evidenced by the pore size distribution graph (inset in Fig. 1e).[16] In addition, Fig. 1f displays the adsorption–desorption isotherm curves and associated pore size distribution charts for all samples, including the raw Mt. Table S2† provides the average pore size, pore volume, and BET surface area for each sample.

X-ray photoelectron spectroscopy (XPS) was used to investigate Mt, BiOCl, and 1B/1M in order to better examine the elemental composition, chemical states, and interactions at the heterojunction interface. The presence of Bi, Cl, O, Si, and Al elements in the survey spectrum of the 1B/1M sample in Fig. 2a indicates that BiOCl was successfully loaded onto the Mt.

The Al 2p and Si 2p XPS spectra of 1B/1M and Mt are illustrated in Fig. 2b and c. The Al 2p and Si 2p XPS spectra of the 1B/1M composite material showed positive changes in binding energy relative to Mt, with shifts of 0.31 and 0.21 eV, respectively. This was consistent with the findings of the FTIR study and showed that the interaction of BiOCl with Mt altered the chemical environment of Si–O–Si and Si–O–Al in Mt.[23] Fig. 2d shows the Bi 4f XPS spectra of 1B/1M and pure BiOCl. Pure BiOCl demonstrated two prominent XPS peaks at 164.66 and 159.34 eV, which could be attributed to Bi^{3+} ions in the Bi $4f_{5/2}$ and Bi $4f_{7/2}$ orbitals, respectively.[34] A slight positive shift of binding energy was observed in the Bi 4f XPS spectrum of the 1B/1M composite material, indicating a change in the density of the electron states surrounding Bi caused by the creation of interface covalent bonds between the hydroxyls of Mt and BiOCl.[35] Similarly, the peaks with binding energies of 199.91 and 198.24 eV could be well assigned to Cl $2p_{1/2}$ and Cl $2p_{3/2}$, respectively, belonging to Cl^- in BiOCl (Fig. 2e). Meanwhile, a slight negative shift in the Cl 2p binding energy was observed in the 1B/1M composite material, providing strong evidence for the chemical bonding between BiOCl and Mt. The O 1s XPS spectra were divided into two major peaks, as seen in Fig. 2f. Peaks at 530.51 and 532.89 eV represented the lattice oxygen in the $[Bi_2O_2]^{2+}$ layer of BiOCl and the surface-adsorbed hydroxyl oxygen, respectively.[36] For the 1B/1M composite material, the peaks were centered at 530.53 and 532.55 eV, and the ratio of the two peaks is significantly increased. This

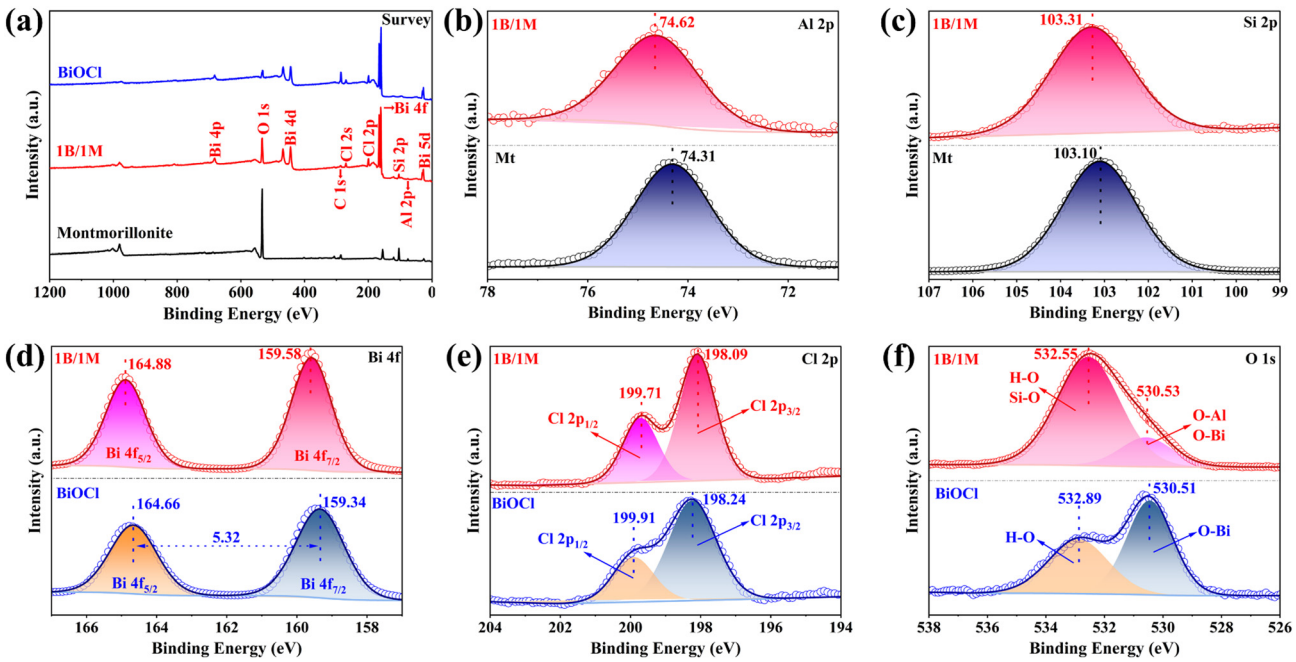

Fig. 2 (a) XPS survey spectra and the high resolution XPS spectrum of (b) Al 2p, (c) Si 2p, (d) Bi 4f, (e) Cl 2p and (f) O 1s.

is because Mt has a lot of O–Si bonds, which have similar binding energies to hydroxyl oxygen, and a slight negative shift in binding energy was observed. The above analysis indicates the occurrence of charge transfer between BiOCl and Mt. Si, Al, and Bi elements lose electrons in the binding process, while Cl and O elements gain electrons. This indicated that the interaction between the two components went beyond a simple physical mixture, leading to the formation of a well-integrated heterojunction. Such a heterojunction structure was beneficial for enhancing the overall performance, reusability, and chemical stability of the 1B/1M composite material.

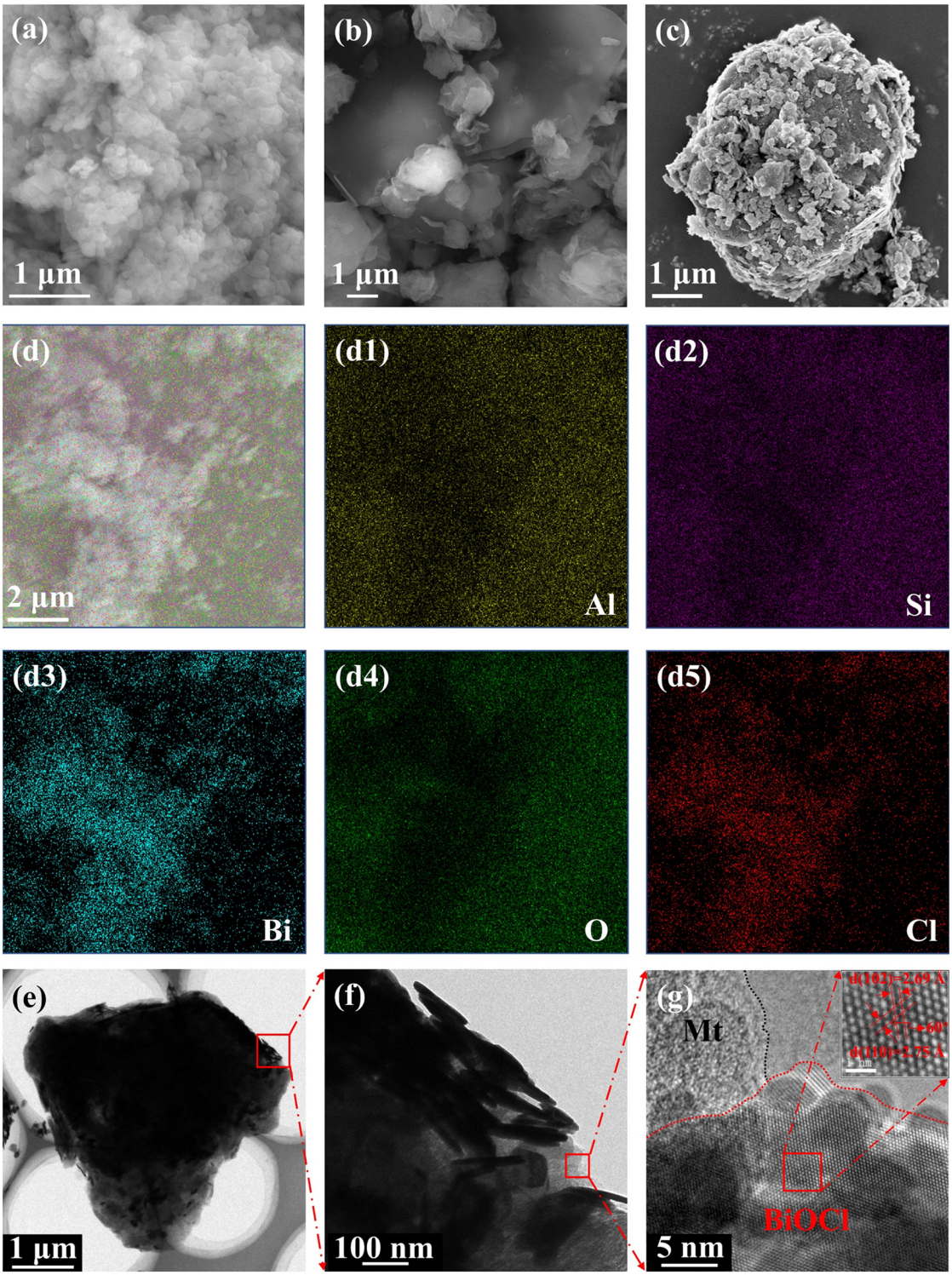

Fig. 3 SEM images of (a) BiOCl, (b) Mt, and (c) 1B/1M. (d and d1–d5) corresponding elemental mapping. (e and f) TEM and (g) HRTEM images of 1B/1M.

The surface morphology and elemental composition of the samples were analyzed using SEM. As shown in Fig. 3a, an image of pure BiOCl nanosheets is presented, exhibiting a planar size of approximately 150 nm and a thickness of around 25 nm, accompanied by severe agglomeration. As shown in Fig. 3b, Mt has an irregular block structure with a size of generally a few micrometers and a relatively smooth surface, which is beneficial for the assembly and synthesis of composites. The EDX spectra and atomic percentages of each element for BiOCl and Mt are provided in the ESI† (Fig. S2 and Tables S3 and S4). Notably, the small amount of Fe in Mt can be attributed to the isomorphic substitution of Fe^{3+} in the Al–O and Si–O sublayers.[37] BiOCl nanosheets were evenly dispersed on the surface of Mt for the 1B/1M composite (Fig. 3c), and the dispersion was much better than that of pure BiOCl. Mt support could effectively inhibit the agglomeration of BiOCl. Furthermore, elemental mapping using EDX spectroscopy revealed that elements such as Al, Si, Bi, O, and Cl were uniformly distributed throughout the 1B/1M composite material (Fig. 3d1–d5). The corresponding EDX spectra (Fig. S3†) and atomic percentages of each element are presented in the ESI† (Table S5). The relevant atomic ratios were also in close agreement with the theoretical stoichiometric ratios, confirming the successful preparation of the 1B/1M composite material.

The microstructure of the 1B/1M composite material was further investigated using TEM and HRTEM methods. As shown in Fig. 3e and f, BiOCl nanosheets were evenly disseminated throughout the surface of the asymmetrically formed Mt. In the HRTEM image (Fig. 3f), distinct lattice fringes are observed with *d*-spacing values of 2.75 Å and 2.69 Å, forming a 60° angle. These lattice fringes corresponded to the (110) and (102) planes of BiOCl, respectively. In addition, the lines in Fig. 3g indicate the formed grain boundaries, which helped to separate and transfer photogenerated charge carriers, thereby improving the overall photocatalytic degradation efficiency.

3.2 Photoelectrochemical (PEC) performance testing

A series of photoelectrochemical (PEC) tests were made in order to look into the separation and transport effectiveness of photoinduced charge carriers in photocatalysts. As shown in Fig. 4a, 1B/1M exhibited the highest transient photocurrent response, indicating its highest efficiency of photogenerated carrier separation. Notably, compared to pure BiOCl, all the composite materials exhibited improved charge carrier separation efficiency. However, the best separation efficiency was shown by 1B/1M, and this was because Mt was loaded properly. Insufficient loading could not effectively improve the aggregation of BiOCl nanosheets, while excessive loading resulted in insufficient charge carriers. Interestingly, we observed that the pristine Mt also exhibited weak photocurrent response, which could be attributed to the Al–O and Si–O sub-layers of Mt.[20] In addition, we performed photoluminescence (PL) analysis and electrochemical impedance spectroscopy (EIS) testing on a range of samples. A lesser resistance to photoinduced carrier transfer inside the system was often indicated by a smaller radius of the semicircular arc shown in the Nyquist plot. This, in turn, signified a stronger charge migration ability of the system.[38,39] 1B/1M has the smallest EIS spectral arc radius (Fig. 4b) and the lowest PL intensity (Fig. 4c), suggesting that its photogenerated carriers are more prone to segregation and have the lowest complexation efficiency. In conclusion, the findings from the analysis of transient photocurrent response, EIS, and PL spectra all indicated that the introduction of Mt could effectively promote the separation of photogenerated carriers and achieve the highest separation efficiency through microscale modulation (including the coordination of component ratios).

3.3 Photocatalytic performance testing

TCH was employed as the target pollutant to evaluate the photocatalytic activity of the produced photocatalysts. As depicted in Fig. 5a, when no photocatalyst was added, the concentration of the TCH solution remained constant under both dark and illuminated conditions. This observation suggests that TCH does not undergo self-degradation. For pristine Mt and pure BiOCl, after 60 minutes of dark adsorption, approximately 58.8% and 3.3% TCH could be adsorbed, respectively, followed by 60 minutes of photocatalytic degradation, which degraded approximately 9.7% and 53.6% TCH, respectively. BiOCl had poor

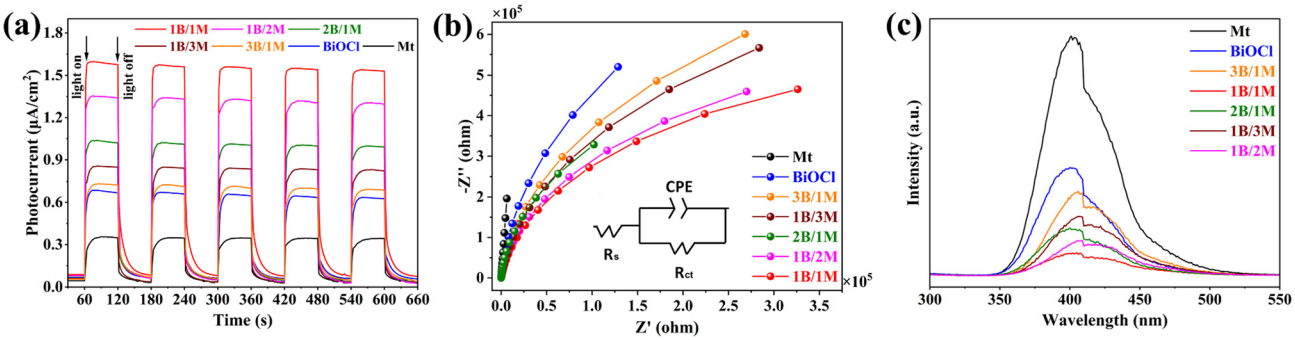

Fig. 4 (a) Transient photocurrent responses, (b) EIS Nyquist plots and (c) PL spectra of several photocatalysts.

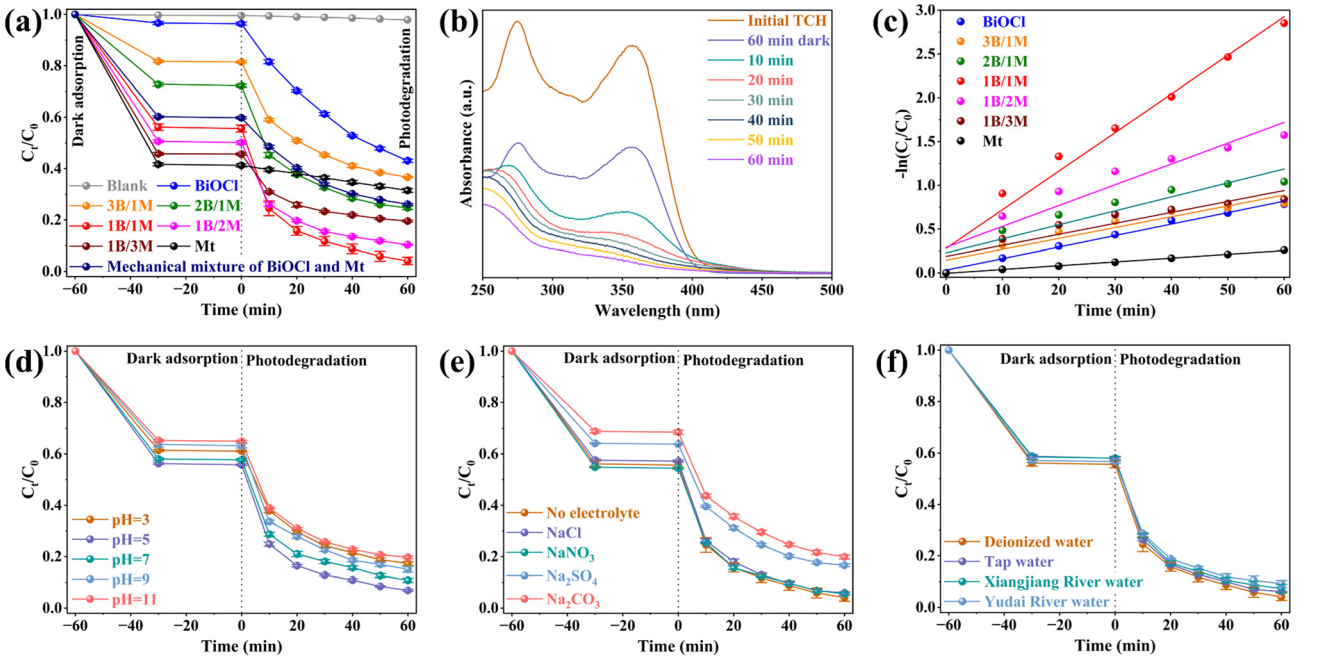

Fig. 5 (a) Adsorption and photocatalytic degradation performance of different photocatalysts for TCH. (b) UV-vis spectra of 1B/1M adsorption and photocatalytic degradation of TCH. (c) First-order kinetic fitting curves for the photocatalytic degradation of TCH using different photocatalysts. Adsorption and photocatalytic degradation performance of 1B/1M on TCH under different external conditions: (d) pH, (e) inorganic ions and (f) different water quality.

adsorption performance for TCH but exhibited excellent photocatalytic properties. In contrast, Mt demonstrated a strong adsorption capacity for TCH, but its photocatalytic performance was unsatisfactory. The adsorption capability for TCH steadily increased for a number of composites as the Mt content rises. However, the overall photocatalytic degradation efficiency reached its maximum when the mass ratio of BiOCl to Mt was 1 : 1. After 60 minutes of dark adsorption and photocatalytic degradation, the final removal rate of TCH reached 95.9% (Fig. 5a and b). Less Mt support could not avoid severe aggregation of BiOCl, resulting in low photogenerated carrier separation efficiency and insufficient active reaction sites. Excess Mt support caused the active substances to decrease, which could not promptly degrade the TCH on the photocatalyst surface. For comparison, pure BiOCl and Mt were mechanically mixed in a 1 : 1 ratio. It was evident that the adsorption capacity and photocatalytic degradation efficiency towards TCH were lower than that of the 1B/1M composite (Fig. 5a), indicating the presence of a synergistic effect in the catalytic degradation of TCH by 1B/1M. In addition, we collected the degradation performance of BiOCl-based photocatalysts for TCH in recent years and showed that our photocatalysts also have significant advantages (Table S6†).

Furthermore, a pseudo-first-order kinetic model with the following equation may be used to investigate the degradation of TCH by various photocatalysts in greater detail: $-\ln(C_t/C_0) = kt$, where C_t is the concentration of TCH at time t, C_0 is the initial concentration of TCH, and k and t represent the reaction rate constant and reaction time, respectively. In Fig. 5c and S4,† the photocatalyst 1B/1M exhibited the highest k value, which was 10.2 times greater than that of Mt and 3.4 times higher than that of pure BiOCl. It was also much greater than that of other loading ratios for composite materials, showing that the kinetics of the photocatalytic process could be significantly improved with the proper loading ratio.

Finally, the effects of varying water quality, inorganic ions, and solution pH on the photocatalytic activity of the 1B/1M sample were also investigated. The effectiveness of TCH degradation was influenced by the pH of the solution because protonation and deprotonation events occur throughout the degradation process in the solution.[21] When the solution was under strong acid conditions (below 3.3), TCH molecules exist in the cationic form (TCH^{3+}) due to the protonation of the dimethylamino group; TCH molecules existed in the zwitterionic state (TCH_2) when the pH of the solution was between 3.3 and 7.7 as a result of the phenolic diketone moiety losing a proton; due to the deprotonation processes of the three carbamoyl system and the phenolic diketone, TCH molecules existed in the anionic state (TCH^-/TC^{2-}) when the solution pH was greater than 7.7.[40] Fig. S5† shows the zeta potential of BiOCl and 1B/1M composite materials as a function of pH. The BiOCl surface carries a positive charge when the pH is below 6, while for the 1B/1M composite material, due to the permanent negative charge on the surface of Mt, it carries a negative charge over a large pH range. As shown in Fig. 5d, a pH of 5 in the solution resulted in the maximum degradation efficiency. However, at solution pH levels of 3 or 11, a noticeable decrease in degradation

efficiency was seen, showing that the photocatalytic process was not favored in these settings. When the pH value was 11, the adsorption performance of 1B/1M for TCH also decreased significantly. Combined with the zeta potential, this may be because of the high electrostatic attraction between the negatively charged 1B/1M composite material and TCH in anionic form in a strongly alkaline environment. The fact that the adsorption performance was still superior to that of pure BiOCl, however, suggests that the surface complexation effect rather than electrostatic attraction played a key role.[41] Overall, the 1B/1M composite material showed good degradation performance for TCH under neutral or weakly acidic/alkaline conditions. Fig. S6† shows the kinetic information of each reaction under different external factors, and we can see that the highest kinetic reaction rate constant was observed at a solution pH of 5, which once again illustrates that mild conditions are more suitable for the degradation of TCH solution.

In fact, many other inorganic salt ions are often present in real wastewater, which could also greatly affect the efficiency of photocatalytic degradation reactions. In this regard, some common inorganic ions such as Na^+, Cl^-, SO_4^{2-}, NO_3^- and CO_3^{2-} were added to the degradation process to investigate their specific effects on the photocatalytic reaction. As shown in Fig. 5e, moderate amounts of Na^+, Cl^- and NO_3^- in solution do not affect the photocatalytic reaction. There was a significant decrease in degradation efficiency due to the fact that SO_4^{2-} competes with TCH molecules for reaction sites.[42] CO_3^{2-} decreases the degradation efficiency, for which there are two possible reasons. Firstly, CO_3^{2-} will undergo hydrolysis to produce OH^- and HCO_3^-, resulting in an alkaline solution. Combined with Fig. 5d we know that an alkaline environment is not conducive to the reaction. Secondly, CO_3^{2-} and HCO_3^- were considered to be scavengers of $^{\cdot}OH$ and their scavenging mechanisms are shown by eqn (1) and (2):

$$CO_3^{2-} + {}^{\cdot}OH \rightarrow CO_3^{\cdot-} + OH^- \quad (1)$$

$$HCO_3^- + {}^{\cdot}OH \rightarrow CO_3^{\cdot-} + H_2O \quad (2)$$

In general, the oxidation potential of $CO_3^{\cdot-}$ radicals was lower than that of $^{\cdot}OH$ radicals.[43] Therefore, the introduction of CO_3^{2-} into the solution resulted in a significant decrease in the degradation efficiency of the 1B/1M composite for TCH molecules.

We have conducted research on the impact of different water qualities on degradation efficiency, selecting three distinct types of tap water, Xiangjiang River water, and Yudai River water. As shown in Fig. 5f, the experimental findings unmistakably show that for all three types of water, the degrading efficiency of the 1B/1M composite material was not considerably lower than that of deionized water. This suggests that the 1B/1M composite material demonstrates excellent adaptability to natural water environments, offering a strong basis for its practical use.

3.4 Band structure analysis

The performance of photocatalysts depends on their ability to absorb light. Fig. 6a shows the UV-vis diffuse reflectance spectra (UV-vis DRS) of Mt, BiOCl and 1B/1M composites,

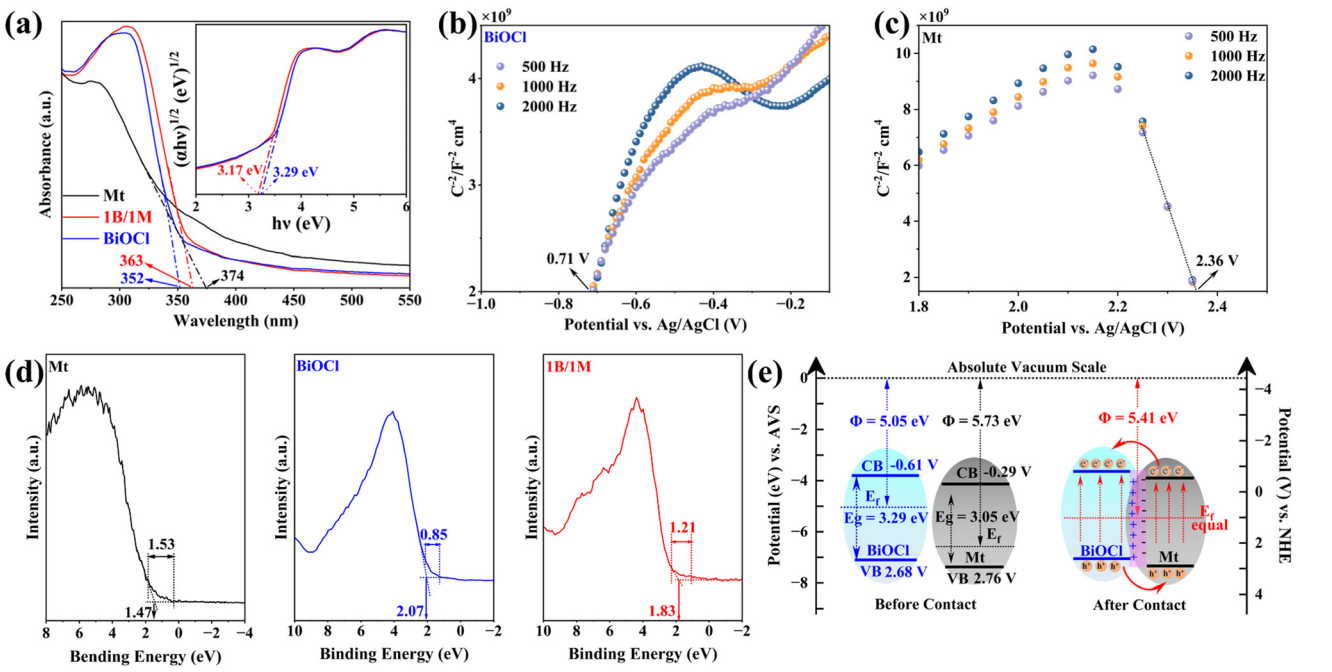

Fig. 6 (a) UV-vis diffuse reflectance spectra and corresponding Tauc plots (inset). M–S plots of (b) BiOCl and (c) Mt. (d) VB-XPS spectra of Mt, BiOCl and 1B/1M. (e) Band structure of BiOCl and Mt before and after contact.

and the absorption edges were located at approximately 374 nm, 352 nm and 363 nm, respectively. The 1B/1M composite exhibited greater light absorption as well as a substantial red-shift in the absorption edge when compared to pure BiOCl. In addition, the bandgaps (E_g) of BiOCl and 1B/1M were determined by the Tauc plot of the Kubelka–Munk function using eqn (3):[44]

$$\alpha h\nu = k(h\nu - E_g)^{n/2} \quad (3)$$

where α is the absorption coefficient, h is Planck's constant, ν is the frequency of light, and k is the proportionality constant. Both BiOCl and 1B/1M can be considered as indirect semiconductors, with n = 4, and Mt can be considered as a direct semiconductor, with n = 1. The E_g values of BiOCl, 1B/1M and Mt were 3.29, 3.17 and 3.05 eV, respectively, as shown in the inset of Fig. 6a and S7.† The reduction of the E_g reduced the minimum energy required for the photocatalytic reaction and facilitated the overall photocatalytic reaction system.

The specific band structures of BiOCl and Mt were analyzed using the Mott–Schottky (M–S) curve (Fig. 6b and c). First, the slope of the M–S curve for BiOCl is positive, indicating that this is an n-type semiconductor, whereas the slope of the M–S curve for Mt is negative, suggesting that Mt exhibits p-type semiconductor properties.[45] In addition, it was observed that the M–S curve of 1B/1M had an inverted "V" shape (Fig. S8†); this demonstrated that a p–n heterojunction formed between the two materials with significant proof.[46] Additionally, the flat-band potentials (E_{fb}) of BiOCl and Mt were found to be −0.71 and 2.36 V, respectively, in relation to the Ag/AgCl reference electrode, which were converted relative to the normal hydrogen electrode by the equation $E_{NHE} = E_{Ag/AgCl} + 0.197$.[47] As a result, it was discovered that the E_{fb} values of BiOCl and Mt were −0.51 and 2.56 V, respectively. The conduction band potential (E_{CB}) for n-type semiconductors was typically 0.1 V more negative than E_{fb}, and the valence band potential (E_{VB}) for p-type semiconductors was typically 0.2 V more positive than E_{fb}.[48] Therefore, the E_{CB} values of BiOCl and the E_{VB} values of Mt were −0.61 and 2.76 V, respectively (Fig. 6e). Subsequently, the E_g values of BiOCl and Mt were 3.29 and 3.05 eV, respectively (Fig. 6a and S7†). Therefore, using the equation $E_g = E_{VB} - E_{CB}$, the E_{VB} of BiOCl and the E_{cB} of Mt were determined to be 2.68 and −0.29 V, respectively. To be more convincing, it was verified by VB-XPS combined with the semiconductor work function. In Fig. 6d, the differences between the Fermi energy levels (E_f) and E_{VB} ($\Delta(E_f, E_{VB})$) were 1.47, 2.07 and 1.83 eV for Mt, BiOCl and 1B/1M, respectively, with respect to the absolute vacuum scale (AVS). At the same time, there is a relationship in the XPS measurements of solids: $h\nu = E_k + E_b + \Phi$, where $h\nu$ represents the energy of the incident photon, E_k is the kinetic energy of the photoelectron, E_b is the binding energy of the electron, and Φ is the work function of the sample. Due to the difference in the work function, the contact potential difference ($\Delta V = \Phi - \varphi$, φ represents the work function of the XPS measuring instrument, φ = 4.2 eV in this study) leads to a change in the kinetic energy of the free electrons and eventually to a change in their binding energy.[49] ΔV can be obtained from the distance of the inflection point in the XPS measurement and the corresponding sample Φ is calculated. Therefore, the Φ of BiOCl, Mt and 1B/1M could be easily obtained as 5.05, 5.73 and 5.41 eV, respectively. The corresponding $E_{VB,\ AVS}$ values are calculated by the formula $E_{VB,\ AVS} = \Phi + \Delta(E_f, E_{VB})$ and then converted into the corresponding potential at the normal hydrogen electrode: E_{NHE} (V) = E_{AVS} (eV) − 4.44.[50] Finally, the E_{VB} values of BiOCl and Mt were 2.68 and 2.76 V, and the E_{CB} values were calculated as −0.61 and −0.29 V, respectively. In conclusion, the results of the two methods were matched successfully.

As mentioned previously, the higher work function of Mt compared to BiOCl indicates that the Fermi energy level of BiOCl is higher than that of Mt. Therefore, when BiOCl and Mt are in contact, electrons will spontaneously flow from the side with the higher Fermi energy level to the side with the lower Fermi energy level until their Fermi energy levels are reequilibrated. At the same time, an internal electric field (IEF) is formed at the interface of the heterojunction pointing from the lower Fermi energy level to the higher Fermi energy level, so that electrons are spontaneously transferred from BiOCl to the surface of Mt, and a new Fermi level equilibrium is established.[51] When 1B/1M is excited by incident light, the electrons in the valence band transition to the conduction band and generate a photogenerated hole, which will rapidly migrate to the surface of Mt under the action of IEF, and the natural negative charge on the surface of Mt due to its intrinsic property also provides a stronger driving force for the migration of positively charged holes. Thus, efficient spatial separation of photogenerated carriers is realized. This resulted in the enhanced photocatalytic degradation performance of 1B/1M.

3.5 Degradation mechanism

Radical trapping experiments were performed in order to look into the mechanism of the photocatalytic reaction and the role of various reactive radicals. The degradation efficiency of TCH decreased by 5.2% when IPA was added to the solution, as shown in Fig. 7a, demonstrating that $^{\cdot}OH$ had only a minimal impact on the process. The degradation efficiency was decreased by 23.9% when LAA was introduced, indicating that $^{\cdot}O_2^-$ was more crucial to the degradation process. Last but not least, the degradation efficiency drastically dropped when EDTA-2Na was added to the solution, going from 96.4% to 37.1%, indicating that h^+ predominated in the degradation reaction. In addition, Fig. S9† provides corresponding kinetic information when different quenchers were added. The obvious weakening of the kinetics, particularly with the addition of EDTA-2Na, further supported the idea that h^+ played the primary role in the degradation mechanism.

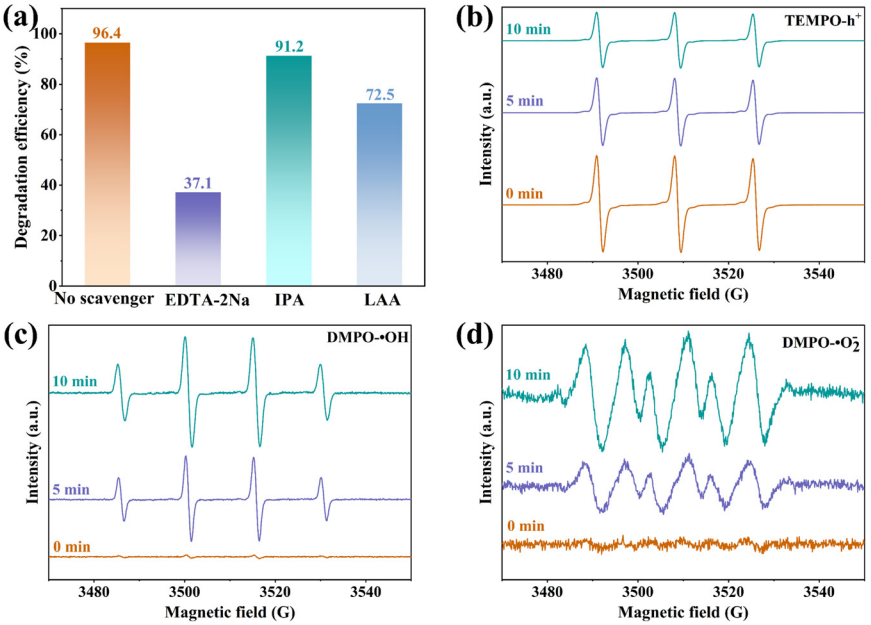

Fig. 7 (a) Effects of different scavengers. ESR spectra of 1B/1M for the signal of (b) TEMPO-h^+, (c) DMPO–$^{\cdot}OH$ and (d) DMPO–$^{\cdot}O_2^-$.

Further confirmation of the presence of free radicals in the reaction was done using the electron spin resonance (ESR) method. In Fig. 7b, the ESR characteristic signal of TEMPO gradually diminished with the increase in illumination time, which was due to the fact that h^+ could oxidize TEMPO, thus determining the presence of h^+. Similarly, DMPO was used to verify the presence of $^{\cdot}OH$ and $^{\cdot}O_2^-$, and it was clear that in the absence of light illumination, no significant characteristic peaks appeared. Upon illumination for 5 minutes, a highly characteristic and discernible signal (1 : 2 : 2 : 1) corresponding to DMPO–$^{\cdot}OH$ radicals was prominently observed (Fig. 7c). Furthermore, with an increase in the illumination time, the relative intensity of this characteristic signal exhibited a significant enhancement. Fig. 7d shows the typical characteristic signal of DMPO–$^{\cdot}O_2^-$ (1 : 1 : 1 : 1), and the relative intensities of both increased significantly with the extension of illumination time, which fully proved that the $^{\cdot}OH$ and $^{\cdot}O_2^-$ were being continuously generated in the reaction system under the irradiation of incident light.

A putative reaction mechanism was suggested in conjunction with the study of the energy band structure of 1B/1M that was done above. First, 1B/1M was excited by incident light and the electron in the valence band jumps to the conduction band. At this point, a photogenerated electron with a reducing character appears in the conduction band, while a photogenerated hole with an oxidizing character is generated in the valence band (eqn (4)). The conduction band potential of 1B/1M (−0.39 V *vs.* NHE) was more negative than that of $O_2/^{\cdot}O_2^-$ (−0.33 V *vs.* NHE), which allows the photogenerated electron to readily convert O_2 to $^{\cdot}O_2^-$ (eqn (5)), according to the band structure analysis (Fig. 6e). Meanwhile, the photogenerated holes may directly oxidize water molecules or OH^- (eqn (6)) ionized from water molecules to $^{\cdot}OH$ (eqn (7) and (8)) due to the valence band potential (2.78 V *vs.* NHE), which was likewise more positive than $OH^-/^{\cdot}OH$ (1.99 V *vs.* NHE) and $H_2O/^{\cdot}OH$ (2.37 V *vs.* NHE). Notably, the photogenerated electrons in the conduction band were quickly moved to the surface of Mt due to the p–n heterojunction created in the 1B/1M system, speeding up the separation of photogenerated carriers. This helped to explain why the h^+ played a prominent role in the 1B/1M system. Eventually, these reactive substances (h^+, $^{\cdot}O_2^-$ and $^{\cdot}OH$) could completely mineralize the TCH molecules to CO_2 and H_2O or degrade them to small molecules (eqn (9)).[52,53]

$$1B/1M + h\nu \rightarrow h^+(VB) + e^-(CB) \quad (4)$$

$$e^-(CB) + O_2 \rightarrow {}^{\cdot}O_2^- \quad (5)$$

$$H_2O \leftrightarrow OH^- + H^+ \quad (6)$$

$$h^+(VB) + H_2O \rightarrow {}^{\cdot}OH + H^+ \quad (7)$$

$$h^+(VB) + OH^- \rightarrow {}^{\cdot}OH \quad (8)$$

$$h^+/{}^{\cdot}O_2^-/{}^{\cdot}OH + TCH \rightarrow CO_2, H_2O \text{ or small molecules} \quad (9)$$

3.6 Degradation path analysis

Fig. S10† demonstrates the mineralization efficiency of 1B/1M for the degradation of TC molecules. As the irradiation time extends, the total organic carbon content in the system gradually decreases, indicating the generation of numerous

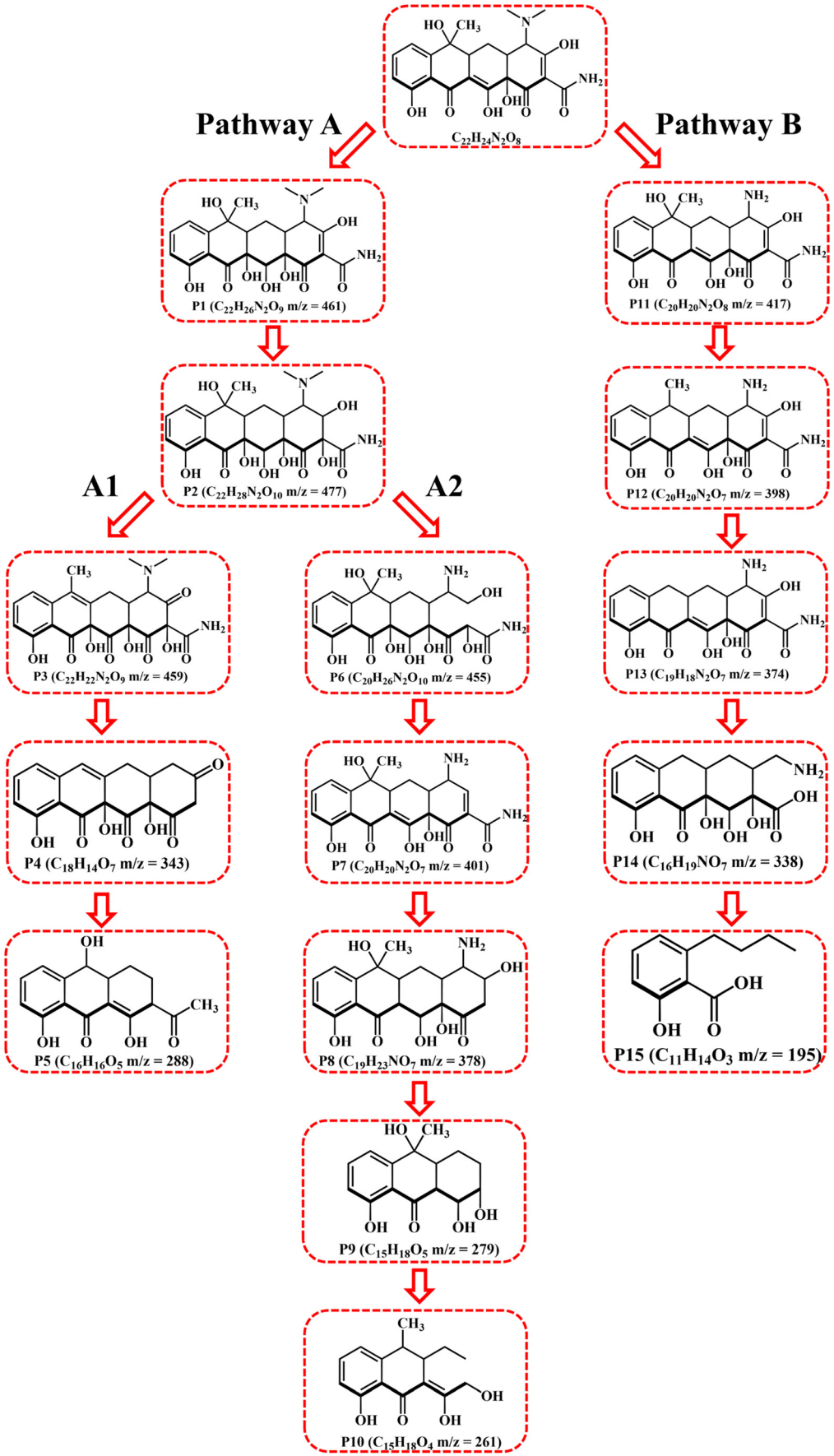

Fig. 8 Possible degradation paths for TC molecules.

intermediates during the degradation process.[15] Therefore, liquid chromatography-mass spectrometry (LC-MS) was employed to investigate the potential degradation pathways of TC molecules and analyze the toxicity of the intermediates produced.

Fig. S11† presents the mass spectrometric data of the pertinent degradation products. Specifically, there are two potential degradation mechanisms (Fig. 8). In general, reactive free radicals and h^+ readily attack highly charged functional groups including double bonds, phenyl groups, amino groups, and acylamino groups.[54] Thus, for pathway A, the TC molecule (m/z = 445) underwent two hydroxylation reactions to form P1 (m/z = 461) and P2 (m/z = 477).[55] There are two possible scenarios at this point. Firstly, P2 generated P3 (m/z = 459) through dehydration,[56] and then P3 underwent a series of reactions, including *N*-demethylation, deamination, dihydroxylation, and deacylation, to produce P4 (m/z = 343).[57] Subsequently, P4 was transformed into P5 (m/z = 288) through ring-opening and dehydroxylation reactions. Second, the combination of Ca^{2+}, Mg^{2+}, and Na^+ in 1B/1M with the $-CONH_2$ of tetracycline increases the $-N(CH_3)_2$ group's deprotonation capacity, making it more susceptible to assault.[58] Therefore, P2 was hydroxylated through ring opening, *N*-demethylation, and addition reactions to form P6 (m/z = 455), which was then dehydroxylated to form P7 (m/z = 401). Subsequently, the acylamino group was attacked to form P8 (m/z = 378), which was further oxidized to form P9 (m/z = 279) and eventually cleaved and dehydroxylated to form P10 (m/z = 261).[59] For pathway B, the TC molecule underwent successive demethylation and dehydroxylation reactions to form P11 (m/z = 417), P12 (m/z = 398), and P13 (m/z = 374).[60] Then, the acylamino group was cleaved and further cleaved and oxidized to form P14 (m/z = 338) and P15 (m/z = 195) through ring opening.[61] Finally, these intermediates could be mineralized to CO_2 and H_2O.

Subsequently, utilizing the computational program ECOSAR, developed by the United States Environmental Protection Agency (EPA), the acute and chronic toxicities of these intermediates to aquatic organisms and the aquatic environment (fish, daphnids, and green algae) were predicted. Fig. 9 shows that the majority of the intermediates were deemed harmless, with over half of them exhibiting toxicities lower than those of the parent TC molecules. Regrettably, a small number of intermediates displayed heightened toxicity, notably the P3 molecule within pathway A1, which exhibited a marked increase in toxicity. Therefore, we explored whether P3 molecules pose a threat to the environment and whether the degradation reaction can maintain continuity, as shown in Fig. S12,† which shows the changes in the concentration of P3 molecules during the degradation process. The signal of P3 molecules appeared firstly when the reaction was carried out up to the 2nd minute and its intensity increased further at the 5th minute, which implies that the rate of P3 molecule production was higher than its consumption in the first 5 minutes of the degradation reaction. As the reaction progresses to the 10th minute, the concentration of P3 molecules decreases, which means that the rate of production of P3 molecules is already lower than the rate of consumption of P3 molecules. By the 15th minute of the reaction, we found that the intensity of P3 molecules became low, and by the 30th minute of the reaction, no signal of P3 molecules could be detected, which means that the P3 molecules have been completely consumed to P4 and P5 molecules, and the toxicity is reduced to harmless. In addition, the concentration of P3 molecules is expected to

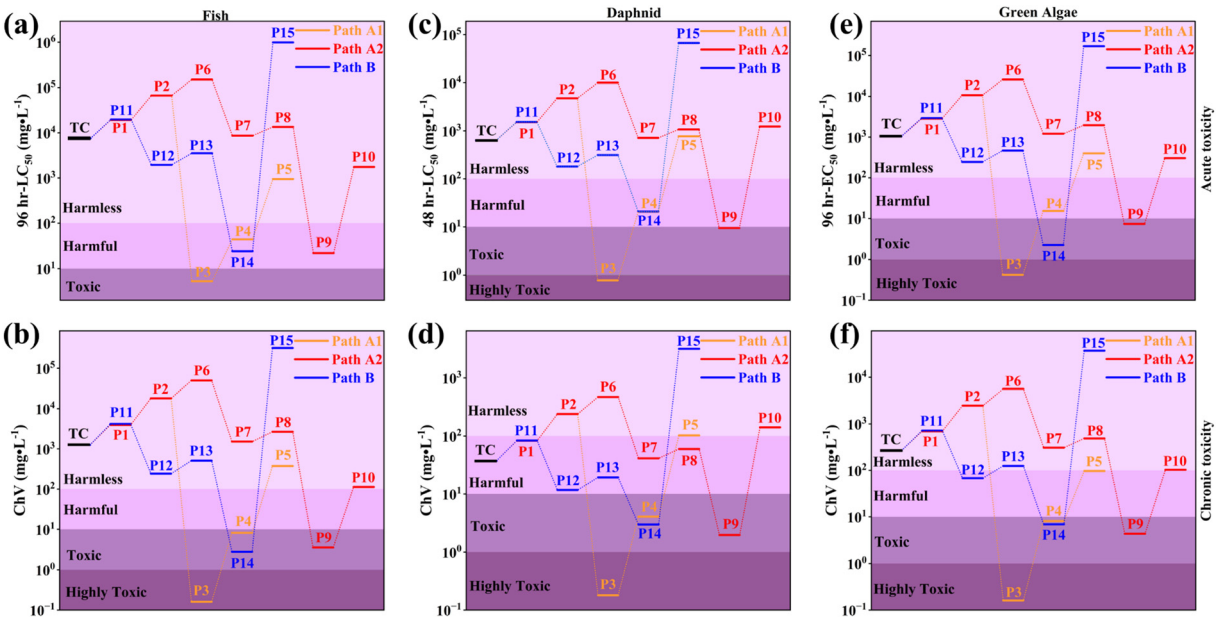

Fig. 9 Predicted acute and chronic toxicity of TC and its intermediates: (a and b) fish, (c and d) daphnids, (e and f) green algae.

remain relatively low throughout the degradation process, so the reaction poses no threat to the environment and continuity can be ensured. In summary, coupled with TOC analysis (Fig. S10†), given ample time, these intermediates were indeed mineralizable into CO_2 and H_2O.

3.7 Stability and scalability testing

The stability and scalability of photocatalysts were two essential indications in real-world applications. Cyclic utilization tests were firstly carried out on 1B/1M. The degrading efficiency of TCH employing 1B/1M did not significantly decline after five cycles of usage testing, as illustrated in Fig. 10a. The removal efficiency of TCH by 1B/1M was as high as 91.5% even in the fifth cycle, showing that it was a superior and reusable photocatalyst. Additionally, the stability of the 1B/1M composite material was further confirmed by XRD, FTIR spectroscopy, and SEM to describe it after usage. In Fig. 10b and c, the intact crystal structure and surface functional groups are shown by the fact that the utilized 1B/1M's XRD and FTIR spectra did not significantly differ from those of the fresh 1B/1M. The BiOCl nanosheets were still firmly attached to the surface of Mt (Fig. 10g). Therefore, 1B/1M exhibited excellent stability and held promising applications in wastewater treatment.

On the other hand, we scaled up the precursor proportion by five and ten times, respectively, as shown in Fig. 10d. As expected, there was no significant difference in the photocatalytic performance of the 1B/1M obtained by scaling up the precursor proportion by five or ten times compared to that obtained using the initial precursor proportion. Similarly, as shown in Fig. 10e and f, the XRD and FTIR spectra were highly consistent with the initial 1B/1M, as expected. Fig. 10h and i show the SEM images of 1B/1M obtained by scaling up the precursor proportion by five or ten times, respectively, and no significant change in the microstructure was observed. These results indicated that obtaining a large amount of photocatalyst by increasing the precursor proportion was feasible.

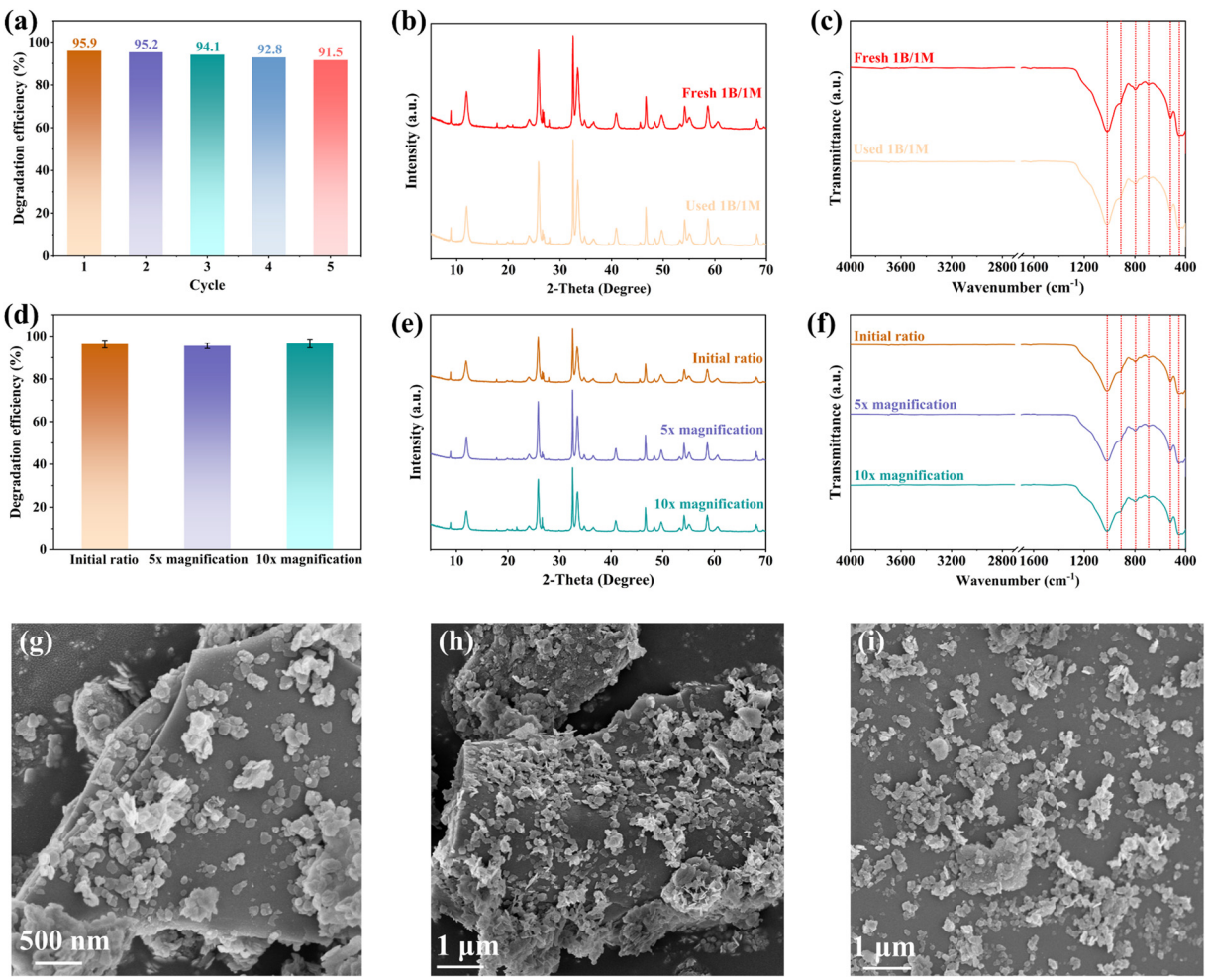

Fig. 10 (a) Cycling performance of 1B/1M. XRD and FTIR spectra of (b) used and (c) fresh 1B/1M. (d) The photocatalytic performance of 1B/1M obtained by expansion and the corresponding (e) XRD and (f) FTIR spectra. (g) SEM image of used 1B/1M and (h and i) 1B/1M obtained by expansion.

4 Conclusions

In conclusion, the electrostatic adsorption and hydrolysis approach was used to create BiOCl/montmorillonite composites in an open container at room temperature. After adjusting the ratio of these two components, the resulting composite material with a 1:1 mass ratio exhibited the strongest photocatalytic degradation performance towards TCH. After 60 minutes of dark adsorption and photocatalytic degradation, the final removal rate of TCH reached 95.9%. Montmorillonite lowered the band gap of BiOCl and created a p–n heterojunction at the interface, which made it easier to separate photogenerated charge carriers, according to band structure analysis and PEC testing. Radical capture and ESR test results indicated that h^+ played a dominant role in the TCH degradation process. Toxicity prediction results revealed that the toxicity of small molecule substances produced during the degradation process was significantly reduced compared to that of TC molecules. Finally, stability and scalability testing showed that 1B/1M was reproducible and scalable. Overall, our research provided evidence that clay minerals, acting as semiconductor carriers, enhanced the efficiency of separating photogenerated carriers and suggested a novel method for producing clay-based photocatalysts on a large scale, at room temperature, and with little energy expenditure.

Conflicts of interest

The authors declare no competing financial interest.

Acknowledgements

This work is supported by the National Natural Science Foundation of China (51674293 and 52274274). The authors would like to thank the Shiyanjia Lab (**https://www.shiyanjia.com**) for the SEM, TEM and ESR tests.

References

1 M. D. K. L. Gunathilaka, S. Bao, X. Liu, Y. Li and Y. Pan, Antibiotic Pollution of Planktonic Ecosystems: A Review Focused on Community Analysis and the Causal Chain Linking Individual- and Community-Level Responses, *Environ. Sci. Technol.*, 2023, **57**, 1199–1213.

2 D. Hu, T. Song, A. Zada, R. Yan, Z. Li, Z. Zhang, J. Bian, Y. Qu and L. Jing, Graphene oxide modulated dual S-scheme ultrathin heterojunctions with iron phthalocyanine and phase-mixed bismuth molybdate as wide visible-light catalysts, *Environ. Sci.: Nano*, 2023, **10**, 922–932.

3 B. Yang, C. Wang, X. Cheng, Y. Zhang, W. Li, J. Wang, Z. Tian, W. Chu, G. V. Korshin and H. Guo, Interactions between the antibiotic tetracycline and humic acid: Examination of the binding sites, and effects of complexation on the oxidation of tetracycline, *Water Res.*, 2021, **202**, 117379.

4 X. Cheng, J. Liao, Y. Xue, Q. Lin, Z. Yang, G. Yan, G. Zeng and A. Sengupta, Ultrahigh-flux and self-cleaning composite membrane based on BiOCl-PPy modified MXene nanosheets for contaminants removal from wastewater, *J. Membr. Sci.*, 2022, **644**, 120188.

5 M. Wei, F. Marrakchi, C. Yuan, X. Cheng, D. Jiang, F. F. Zafar, Y. Fu and S. Wang, Adsorption modeling, thermodynamics, and DFT simulation of tetracycline onto mesoporous and high-surface-area NaOH-activated macroalgae carbon, *J. Hazard. Mater.*, 2022, **425**, 127887.

6 W. Sun, D. Yue, J. Song and Y. Nie, Adsorption removal of refractory organic matter in bio-treated municipal solid waste landfill leachate by anion exchange resins, *Waste Manage.*, 2018, **81**, 61–70.

7 S. Yang, Y. Feng, D. Gao, X. Wang, N. Suo, Y. Yu and S. Zhang, Electrocatalysis degradation of tetracycline in a three-dimensional aeration electrocatalysis reactor (3D-AER) with a flotation-tailings particle electrode (FPE): Physicochemical properties, influencing factors and the degradation mechanism, *J. Hazard. Mater.*, 2021, **407**, 124361.

8 S. Sha, Z. Dong, Y. Gao, H. Hashim, C. T. Lee and C. Li, In-situ removal of residual antibiotics (enrofloxacin) in recirculating aquaculture system: Effect of ultraviolet photolysis plus biodegradation using immobilized microbial granules, *J. Cleaner Prod.*, 2022, **333**, 130190.

9 K. Gao, L.-A. Hou, X. An, D. Huang and Y. Yang, BiOBr/MXene/gC_3N_4 Z-scheme heterostructure photocatalysts mediated by oxygen vacancies and MXene quantum dots for tetracycline degradation: Process, mechanism and toxicity analysis, *Appl. Catal., B*, 2023, **323**, 122150.

10 M. Guan, C. Xiao, J. Zhang, S. Fan, R. An, Q. Cheng, J. Xie, M. Zhou, B. Ye and Y. Xie, Vacancy Associates Promoting Solar-Driven Photocatalytic Activity of Ultrathin Bismuth Oxychloride Nanosheets, *J. Am. Chem. Soc.*, 2013, **135**, 10411–10417.

11 X. Bai, T. Jia, H. Li, L. Guo, M. Jian, Y. Gong, J. Li, Z. Wei and D. Hao, Efficient molecular oxygen utilization of micelle-based BiOCl for enhanced in situ H_2O_2 production induced photocatalytic removal of antibiotics, *Environ. Sci.: Nano*, 2023, **10**, 145–157.

12 D. Zhang, C. Su, S. Yao, H. Li, X. Pu and Y. Geng, Facile in situ chemical transformation synthesis, boosted charge separation, and increased photocatalytic activity of $BiPO_4$/BiOCl p-n heterojunction photocatalysts under simulated sunlight irradiation, *J. Phys. Chem. Solids*, 2020, **147**, 109630.

13 W. Ouyang, F. Teng and X. Fang, High Performance BiOCl Nanosheets/TiO_2 Nanotube Arrays Heterojunction UV Photodetector: The Influences of Self-Induced Inner Electric Fields in the BiOCl Nanosheets, *Adv. Funct. Mater.*, 2018, **28**, 1707178.

14 X. Yao, X. Jiang, D. Zhang, S. Lu, M. Wang, S. Pan, X. Pu, J. Liu and P. Cai, Achieving improved full-spectrum responsive 0D/3D $CuWO_4$/BiOBr:Yb^{3+},Er^{3+} photocatalyst with synergetic effects of up-conversion, photothermal effect and direct Z-scheme heterojunction, *J. Colloid Interface Sci.*, 2023, **644**, 95–106.

15 S. Zhang, Q. Wang, P. Zhang, J. Wang, Y. Li, C. Lu, M. T. Sarwar, X. Dong, Q. Zhao and A. Tang, *et al.*, Nanoclay-

Modulated Interfacial Chemical Bond and Internal Electric Field at the Co3O4/TiO2 p-n Junction for Efficient Charge Separation, *Small*, 2023, **19**, 2300770.

16 S. Zhang, L. Zhong, J. Wang, A. Tang and H. Yang, Porous carbon-based $MgAlF_5{\cdot}1.5H_2O$ composites derived from carbon-coated clay presenting super high adsorption capacity for Congo Red, *Chem. Eng. J.*, 2021, **406**, 126784.

17 S. Zhang, L. Zhong, H. Yang, A. Tang and X. Zuo, Magnetic carbon-coated palygorskite loaded with cobalt nanoparticles for Congo Red removal from waters, *Appl. Clay Sci.*, 2020, **198**, 105856.

18 C. Xu, F. L. Gu and H. Wu, BiOCl-montmorillonite as a photocatalyst for highly efficient removal of Rhodamine B and Orange G: Importance of the acidity and dissolved oxygen, *Appl. Clay Sci.*, 2017, **147**, 28–35.

19 H. H. Naing, Y. Li, J. B. Ghasemi, J. Wang and G. Zhang, Enhanced visible-light-driven photocatalysis of in-situ reduced of bismuth on BiOCl nanosheets and montmorillonite loading: Synergistic effect and mechanism insight, *Chemosphere*, 2022, **304**, 135354.

20 D. Jiang, J. Wang, R. Gao, L. Fu and H. Yang, Contrasting Photochemical Activity of Two Sub-layers for Natural 2D Nanoclay with an Asymmetric Layer Structure, *ACS Appl. Mater. Interfaces*, 2021, **13**, 59431–59439.

21 Z. Guan, X. Li, Y. Wu, Z. Chen, X. Huang, D. Wang, Q. Yang, J. Liu, S. Tian and X. Chen, *et al.*, AgBr nanoparticles decorated 2D/2D GO/Bi2WO6 photocatalyst with enhanced photocatalytic performance for the removal of tetracycline hydrochloride, *Chem. Eng. J.*, 2021, **410**, 128283.

22 X. Hu, C. Li, Z. Sun, J. Song and S. Zheng, Enhanced photocatalytic removal of indoor formaldehyde by ternary heterogeneous $BiOCl/TiO_2$/sepiolite composite under solar and visible light, *Build. Environ.*, 2020, **168**, 106481.

23 X. Liu, W. Wang, C. Du and Y. Su, Synergistic activation of peroxymonosulfate via oxygen vacancy-rich $Co_xMn_{3-x}O_4$/montmorillonite catalyst for environmental remediation, *Appl. Clay Sci.*, 2022, **228**, 106625.

24 C. Lu, S. Zhang, J. Wang, X. Zhao, L. Zhang, A. Tang, X. Dong, L. Fu and H. Yang, Efficient activation of peroxymonosulfate by iron-containing mesoporous silica catalysts derived from iron tailings for degradation of organic pollutants, *Chem. Eng. J.*, 2022, **446**, 137044.

25 P. P. Tun, J. Wang, T. T. Khaing, X. Wu and G. Zhang, Fabrication of functionalized plasmonic Ag loaded Bi_2O_3/montmorillonite nanocomposites for efficient photocatalytic removal of antibiotics and organic dyes, *J. Alloys Compd.*, 2020, **818**, 152836.

26 B. Tyagi, C. D. Chudasama and R. V. Jasra, Determination of structural modification in acid activated montmorillonite clay by FT-IR spectroscopy, *Spectrochim. Acta, Part A*, 2006, **64**, 273–278.

27 I. Ardelean, S. Cora and D. Rusu, EPR and FT-IR spectroscopic studies of Bi_2O_3–B_2O_3–CuO glasses, *Phys. B*, 2008, **403**, 3682–3685.

28 F. Samimi, M. Ghiyasiyan-Arani and M. Salavati-Niasari, New avenue for preparation of potential hydrogen storage materials based on K10 montmorillonite and $Ca_2Mn_3O_8$/$CaMn_3O_6$ nanocomposites, *Fuel*, 2022, **320**, 123933.

29 Y. Wang, Q. Yang, X. Wang, J. Yang, Y. Dai, Y. He, W. Chen and W. Zhang, Photocatalytic degradation of rhodamin B and diclofenac sodium on hollow hierarchical microspheres of BiOBr modified with sepiolite and polyvinyl pyrrolidone (PVP), *Mater. Sci. Eng., B*, 2019, **244**, 12–22.

30 C. Lu, H. Yang, J. Wang, Q. Tan and L. Fu, Utilization of iron tailings to prepare high-surface area mesoporous silica materials, *Sci. Total Environ.*, 2020, **736**, 139483.

31 B. Coasne, A. Grosman, C. Ortega and M. Simon, Adsorption in Noninterconnected Pores Open at One or at Both Ends: A Reconsideration of the Origin of the Hysteresis Phenomenon, *Phys. Rev. Lett.*, 2002, **88**, 256102.

32 S. Zhang, L. Zhong, Z. Xu, J. Hu, A. Tang and X. Zuo, Mineral-modulated Co catalyst with enhanced adsorption and dissociation of BH_4^- for hydrogenation of p-nitrophenol to p-aminophenol, *Chemosphere*, 2022, **291**, 132871.

33 K. Peng, L. Fu, J. Ouyang and H. Yang, Emerging Parallel Dual 2D Composites: Natural Clay Mineral Hybridizing MoS_2 and Interfacial Structure, *Adv. Funct. Mater.*, 2016, **26**, 2666–2675.

34 M. Z. Shahid, Y. Wei, J. Wang, G. Chen, D. Gao, C. Ye, Y. Sun, G.-N. Liu and C. Li, Poly(sodium 4-styrenesulfonate) Assisted Room-Temperature Synthesis for the Mass Production of Bismuth Oxychloride Ultrathin Nanoplates with Enhanced Photocatalytic Activity, *ChemPlusChem*, 2019, **84**, 828–837.

35 Y. Zhou, S. Sun, S. Xi, Y. Duan, T. Sritharan, Y. Du and Z. J. Xu, Superexchange Effects on Oxygen Reduction Activity of Edge-Sharing $[Co_xMn_{1-x}O_6]$ Octahedra in Spinel Oxide, *Adv. Mater.*, 2018, **30**, 1705407.

36 D. Cui, L. Wang, K. Xu, L. Ren, L. Wang, Y. Yu, Y. Du and W. Hao, Band-gap engineering of BiOCl with oxygen vacancies for efficient photooxidation properties under visible-light irradiation, *J. Mater. Chem. A*, 2018, **6**, 2193–2199.

37 D. Jiang, Z. Liu, L. Fu, H. Jing and H. Yang, Efficient Nanoclay-Based Composite Photocatalyst: The Role of Nanoclay in Photogenerated Charge Separation, *J. Phys. Chem. C*, 2018, **122**, 25900–25908.

38 Y. Yang, X. Gu, K. Gong, S. Meng, J. Lei, X. Zheng, Y. Feng and S. Chen, Revealing the charge transfer mechanism and assessing product toxicity in the 2D/1D $Bi_2O_2CO_3/Bi_8(CrO_4)O_{11}$ heterostructure system, *Environ. Sci.: Nano*, 2023, **10**, 1867–1882.

39 X. Jiang, D. Kong, B. Luo, M. Wang, D. Zhang and X. Pu, Preparation of magnetically retrievable flower-like AgBr/$BiOBr/NiFe_2O_4$ direct Z-scheme heterojunction photocatalyst with enhanced visible-light photoactivity, *Colloids Surf., A*, 2022, **633**, 127880.

40 A. Maged, J. Iqbal, S. Kharbish, I. S. Ismael and A. Bhatnagar, Tuning tetracycline removal from aqueous solution onto activated 2:1 layered clay mineral: Characterization, sorption and mechanistic studies, *J. Hazard. Mater.*, 2020, **384**, 121320.

41 D. Huang, J. Li, G. Zeng, W. Xue, S. Chen, Z. Li, R. Deng, Y. Yang and M. Cheng, Facile construction of hierarchical

flower-like Z-scheme AgBr/Bi_2WO_6 photocatalysts for effective removal of tetracycline: Degradation pathways and mechanism, *Chem. Eng. J.*, 2019, **375**, 121991.

42 S. Li, C. Wang, Y. Liu, M. Cai, Y. Wang, H. Zhang, Y. Guo, W. Zhao, Z. Wang and X. Chen, Photocatalytic degradation of tetracycline antibiotic by a novel $Bi_2Sn_2O_7/Bi_2MoO_6$ S-scheme heterojunction: Performance, mechanism insight and toxicity assessment, *Chem. Eng. J.*, 2022, **429**, 132519.

43 R. Zhang, P. Sun, T. H. Boyer, L. Zhao and C.-H. Huang, Degradation of Pharmaceuticals and Metabolite in Synthetic Human Urine by UV, UV/H_2O_2, and UV/PDS, *Environ. Sci. Technol.*, 2015, **49**, 3056–3066.

44 J. Tauc, Optical properties and electronic structure of amorphous Ge and Si, *Mater. Res. Bull.*, 1968, **3**, 37–46.

45 H. Zhang, M. Jia, J. Tong, H. Peng, Y. Xiang, Z. Chen, Z. Xu, Z. Yang and W. Xiong, Coupling effects between metal–organic framework derivatives and oxygen-deficient TiO_2 nanotubes: identified charge-transfer processes and photoelectric synergistic effect, *Environ. Sci.: Nano*, 2023, **10**, 1993–2009.

46 X. Zhang, H. Zhang, J. Yu, Z. Wu and Q. Zhou, Preparation of flower-like Co_3O_4 QDs/Bi_2WO_6 p-n heterojunction photocatalyst and its degradation mechanism of efficient visible-light-driven photocatalytic tetracycline antibiotics, *Appl. Surf. Sci.*, 2022, **585**, 152547.

47 C. Zhou, C. Lai, P. Xu, G. Zeng, D. Huang, Z. Li, C. Zhang, M. Cheng, L. Hu and J. Wan, *et al.*, Rational Design of Carbon-Doped Carbon Nitride/Bi12O17Cl2 Composites: A Promising Candidate Photocatalyst for Boosting Visible-Light-Driven Photocatalytic Degradation of Tetracycline, *ACS Sustainable Chem. Eng.*, 2018, **6**, 6941–6949.

48 D. Zhang, R. Zhang, J. Liu, X. Pu and P. Cai, 3D/2D $ZnIn_2S_4$/$BiFeO_3$ as S-scheme heterojunction photocatalyst for boosted visible-light hydrogen evolution, *J. Am. Ceram. Soc.*, 2023, **106**, 4785–4793.

49 S. Braun, W. R. Salaneck and M. Fahlman, Energy-Level Alignment at Organic/Metal and Organic/Organic Interfaces, *Adv. Mater.*, 2009, **21**, 1450–1472.

50 S. Nazari, E. Asgari, A. Sheikhmohammadi, S. A. Mokhtari and H. Alamgholiloo, Visible-light-driven photocatalytic activity of WO_3/ZIF-67 S-scheme heterojunction for upgrading degradation of oxytetracycline, *J. Environ. Chem. Eng.*, 2023, **11**, 110393.

51 J. Xiong, X. Li, J. Huang, X. Gao, Z. Chen, J. Liu, H. Li, B. Kang, W. Yao and Y. Zhu, CN/rGO@BPQDs high-low junctions with stretching spatial charge separation ability for photocatalytic degradation and H_2O_2 production, *Appl. Catal., B*, 2020, **266**, 118602.

52 Y. Li, S. Yi, R. Duan, S. Li, Z. Sun, J. Shi and L. Gao, Enhanced photocatalytic performance of $Na_{1.8}Zn_{2.1}Mo_3O_{12}$/g-$C_3N_4$ heterojunction for tetracycline degradation, *J. Environ. Chem. Eng.*, 2023, **11**, 110471.

53 Y. Li, J. Geng, Z. Wang, S. Wang and M. Wang, Boosting visible-light photocatalytic tetracycline degradation by constructing core-shell NFO@CN heterostructure, *J. Alloys Compd.*, 2023, **939**, 168635.

54 J. Yang, J. Sun, S. Chen, D. Lan, Z. Li, Z. Li, J. Wei, Z. Yu, H. Zhu and S. Wang, *et al.*, S-scheme 1 T phase $MoSe_2$/AgBr heterojunction toward antibiotic degradation: Photocatalytic mechanism, degradation pathways, and intermediates toxicity evaluation, *Sep. Purif. Technol.*, 2022, **290**, 120881.

55 X. Wu, X. Wang, Y. Xie, N. Ren, J. Ma and P. Ning, Facile in-situ construction of highly dispersed nano zero-valent iron modified black TiO_2 Z-scheme recyclable heterojunction with highly efficient visible-light-driven photocatalytic activity, *Appl. Catal., B*, 2022, **310**, 121325.

56 K. Shi, J. Wang, L. Yin, Y. Xu, D. Kong, H. Li, Y. Zhang, H. He, S. Yang and L. Ni, *et al.*, Photocatalysis Combined with Microalgae to Promote the Degradation and Detoxification of Tetracycline Hydrochloride, *Bull. Environ. Contam. Toxicol.*, 2023, **110**, 43.

57 W. Wang, Z. Li, K. Wu, G. Dai, Q. Chen, L. Zhou, J. Zheng, L. Ma, G. Li and W. Wang, *et al.*, Novel Ag-bridged dual Z-scheme g-C3N4/BiOI/AgI plasmonic heterojunction: Exceptional photocatalytic activity towards tetracycline and the mechanism insight, *J. Environ. Sci.*, 2023, **131**, 123–140.

58 Z. Wu, M. Wang, Y. Bai, H. Song, J. Lv, X. Mo, X. Li and Z. Lin, Upcycling of nickel iron slags to hierarchical self-assembled flower-like photocatalysts for highly efficient degradation of high-concentration tetracycline, *Chem. Eng. J.*, 2023, **464**, 142532.

59 L. Yang, J. Wang, Y. Zhang, B. Zhou, P. Tan and J. Pan, Construction of S-scheme BiOCl/CdS composite for enhanced photocatalytic degradation of antibiotic, *J. Mater. Sci.: Mater. Electron.*, 2022, **33**, 13303–13315.

60 C. Fu, G. Sun, G. Yin, C. Wang, G. Ran and Q. Song, P/N co-doped carbon sheet for peroxymonosulfate activation: Edge sites enhanced adsorption and subsequent electron transfer, *Sep. Purif. Technol.*, 2022, **292**, 120922.

61 J. Gu, C. Ban, J. Meng, Q. Li, X. Long, X. Zhou, N. Liu and Z. Li, Construction of dual Z-scheme UNiMOF/$BiVO_4$/S-C_3N_4 photocatalyst for visible-light photocatalytic tetracycline degradation and Cr(VI) reduction, *Appl. Surf. Sci.*, 2023, **611**, 155575.

